STRUCTURAL SCIENCE
CRYSTAL ENGINEERING
MATERIALS

Volume 74 (2018)

Supporting information for article:

Positive and negative monoclinic deformation of corundum-type trigonal crystal structures of *M*2O3 metal oxides

Piotr Fabrykiewicz, Radosław Przeniosło, Izabela Sosnowska and François Fauth

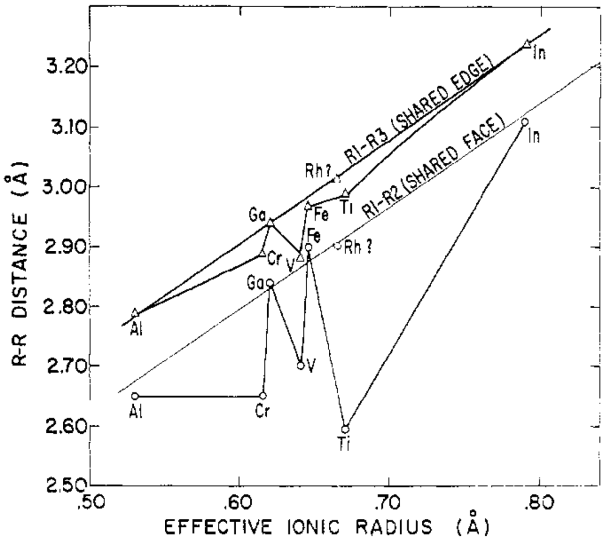

Figure S1: [Copy of Figure 5 from [1]] Metal-metal distances vs. effective ionic radius for M_2O_3 oxides with corrundum-type structures.

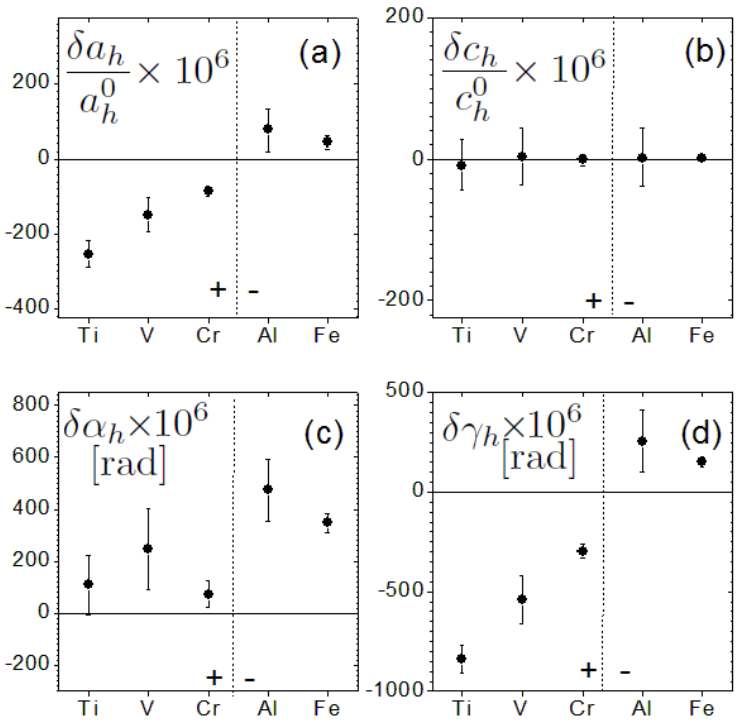

Figure S2: Changes of lattice parameters between hexagonal (index '0') and the pseudo-hexagonal (index '1') system. For a_h and c_h the relative changes are given, e.g. $\delta a_h/a_h^0 = (a_h^1 - a_h^0)/a_h^0$, for α_h and γ_h angles the differences are given in radians, e.g. $\delta\alpha_h = \alpha_h^1 - \alpha_h^0$ (see Table 2). 'Positively' and 'negatively' distorted M_2O_3 oxides (see text) are located on the left and right sides of the vertical dotted line, respectively.

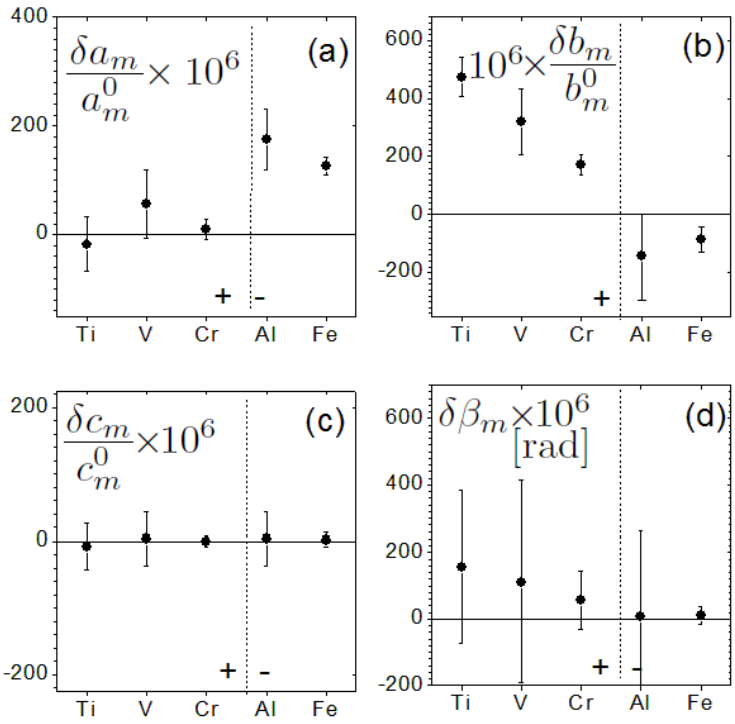

Figure S3: Changes of lattice parameters between the 'undistorted' (index '0') and monoclinic 'distorted' (index '1') system. For a_m, b_m and c_m the relative changes are given, e.g. $\delta a_m/a_m^0 = (a_m^1 - a_m^0)/a_m^0$, for the angle β_m the difference $\delta\beta_m = \beta_m^1 - \beta_m^0$ is given in radians (see Table 2). 'Positively' and 'negatively' distorted M_2O_3 oxides (see text) are located on the left and right sides of the vertical dotted line, respectively.

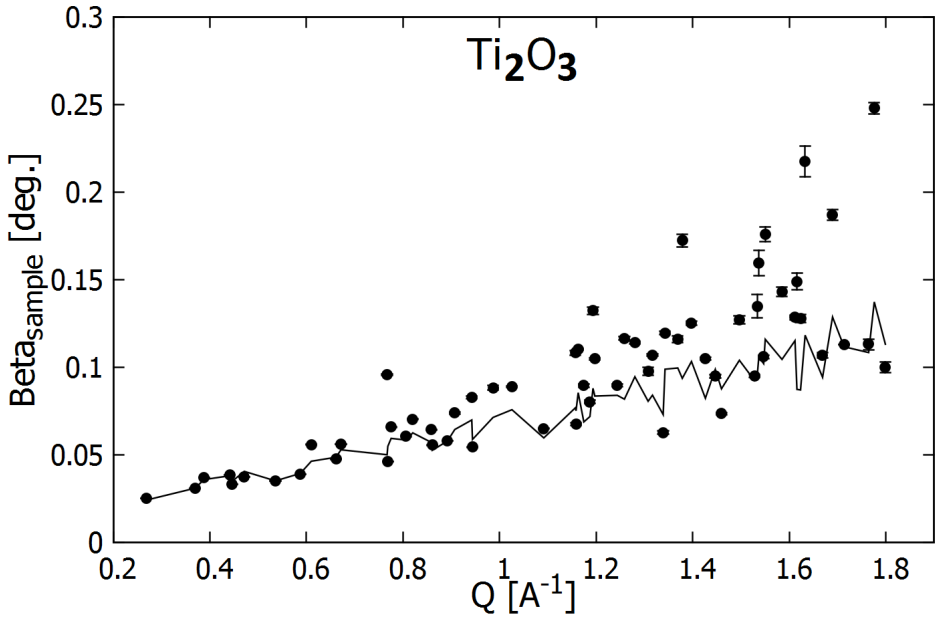

Figure S4: Integral breadth for Ti_2O_3 obtained from model independent fit of experimental SR diffraction patterns (solid symbols) is compared with the $\beta_{sample}(Q)$ values obtained from the anisotropic peak broadening model, eq. 2 (see text).

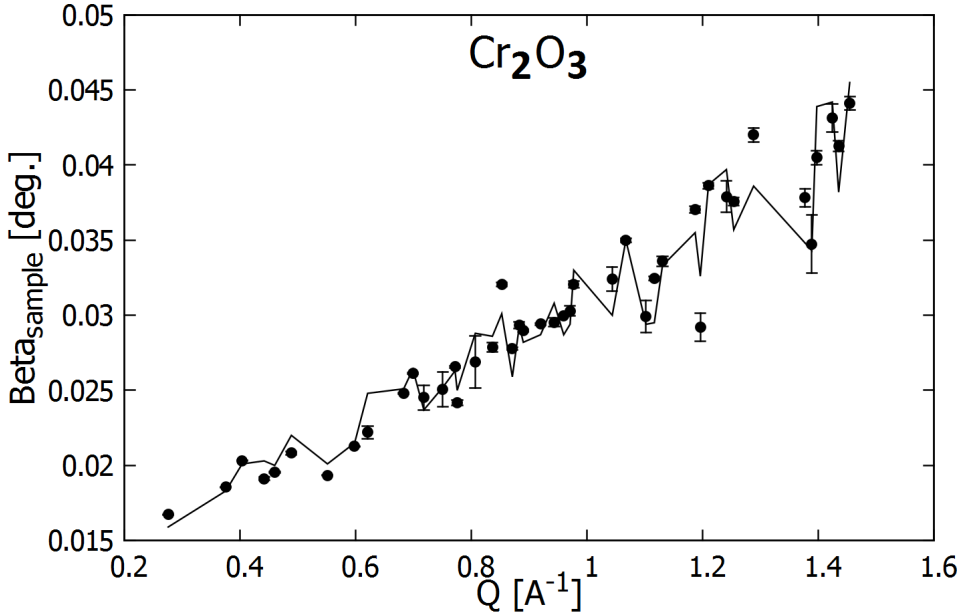

Figure S5: Integral breadth for Cr_2O_3 obtained from model independent fit of experimental SR diffraction patterns (solid symbols) is compared with the $\beta_{sample}(Q)$ values obtained from the anisotropic peak broadening model, eq. 2 (see text).

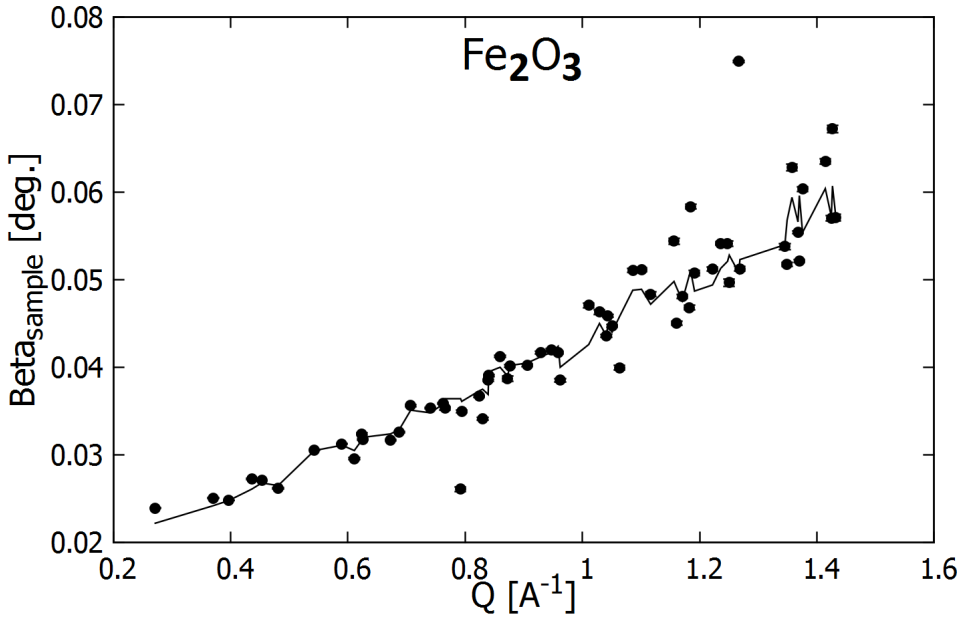

Figure S6: Integral breadth for α-Fe_2O_3 obtained from model independent fit of experimental SR diffraction patterns (solid symbols) is compared with the $\beta_{sample}(Q)$ values obtained from the anisotropic peak broadening model, eq. 2 (see text).

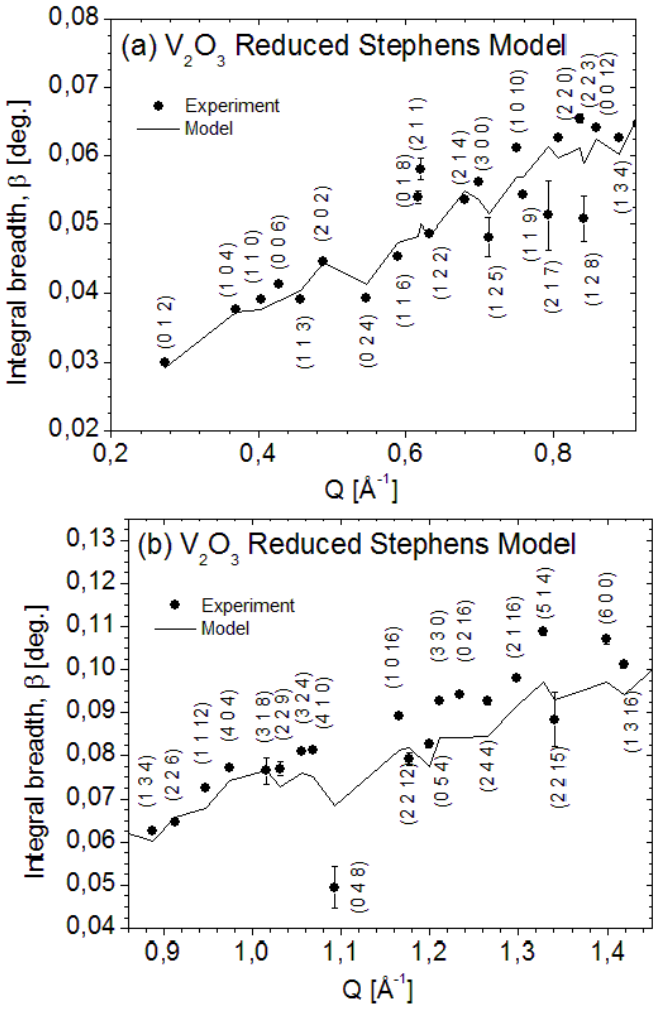

Figure S7: Integral breadths $\beta(Q)$ observed for the Bragg peaks measured with V_2O_3, sample 1 is shown with solid symbols. The reasults of the reduced Stephens model (see eq. 8, i.e. A_1=A_2=A_3=0) are given with the broken line. The measured Q-range is shown in two panels for better visualization. The hexagonal indices within the space group $R\bar{3}c$ are presented.

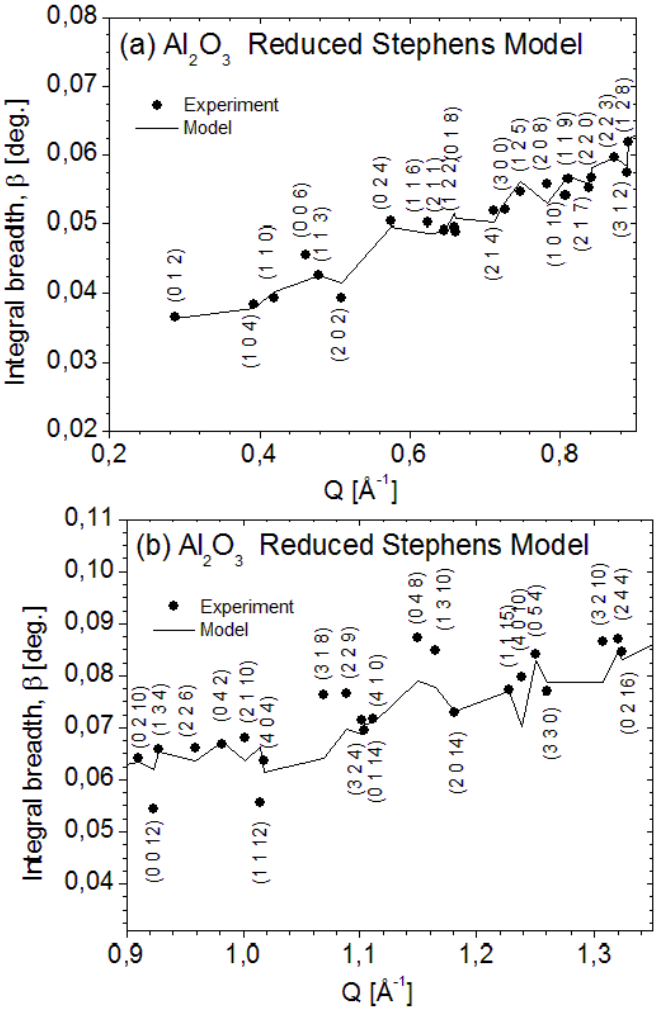

Figure S8: Integral breadths $\beta(Q)$ observed for the Bragg peaks measured with Al_2O_3 is shown with solid symbols. The reasults of the reduced Stephens model (see eq. 8, i.e. A_1=A_2=A_3=0) are given with the broken line. The measured Q-range is shown in two panels for better visualization. The hexagonal indices within the space group $R\bar{3}c$ are presented.

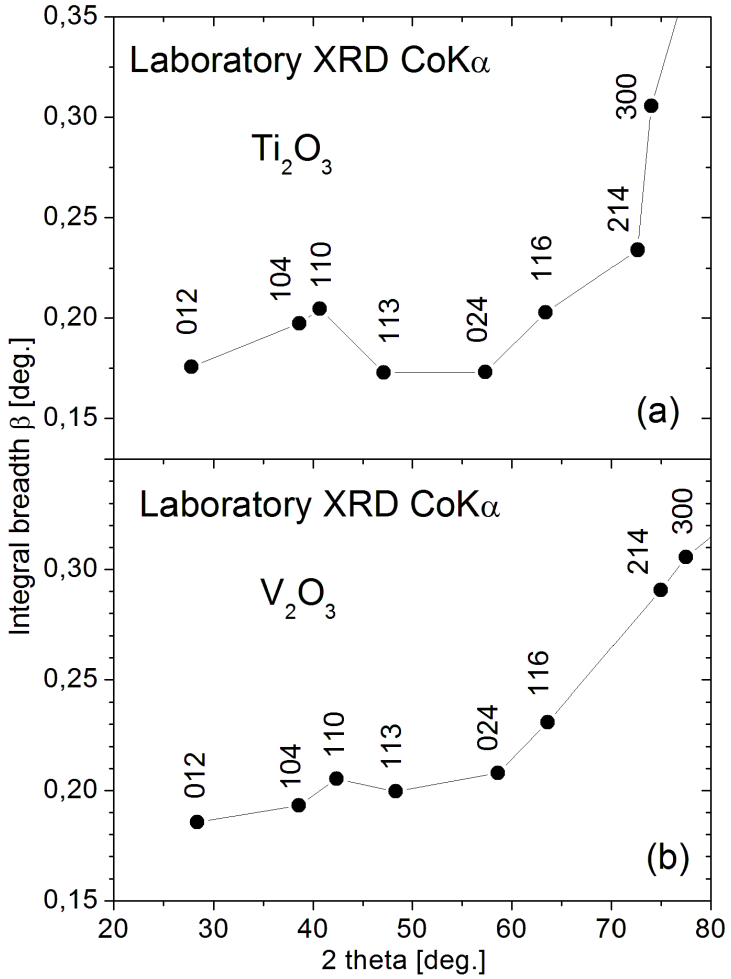

Figure S9: Integral breadths $\beta(2\theta)$ observed for the Bragg peaks measured with (a) Ti_2O_3 and (b) V_2O_3 samples by using the laboratory XRD (Co Kα) setup. The broken lines are shown to guide-the-eye. In both panels (024) peak is below the trend determined by neighbouring Bragg peaks.

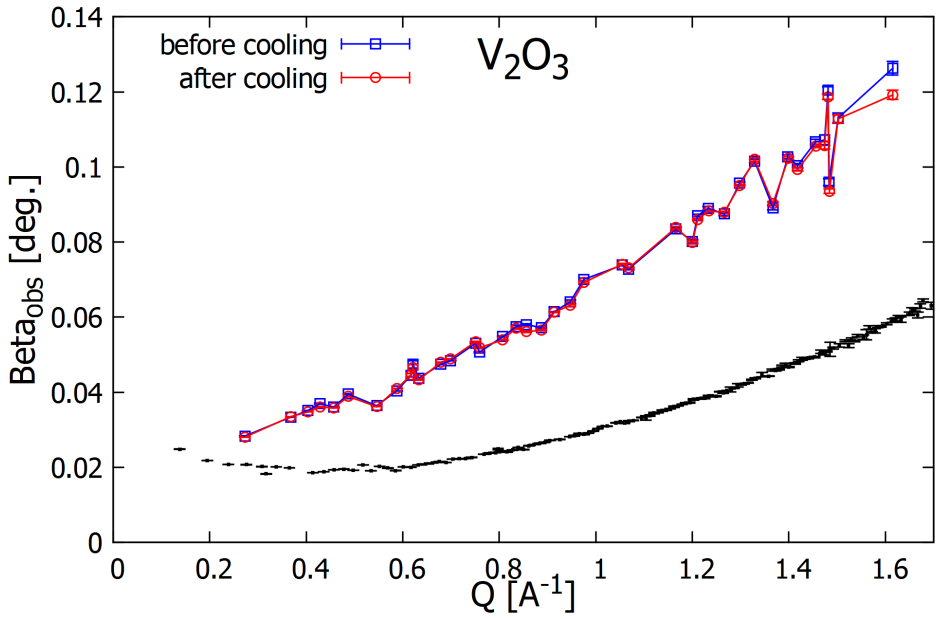

Figure S10: Integral breadths $\beta(Q)$ observed for the Bragg peaks measured with the same V_2O_3 sample before and after cooling to 110 K. Integral breadths $\beta(Q)$ observed for the $Na_2Ca_3Al_2F_{14}$ are presented. The broken lines are shown to guide-the-eye.

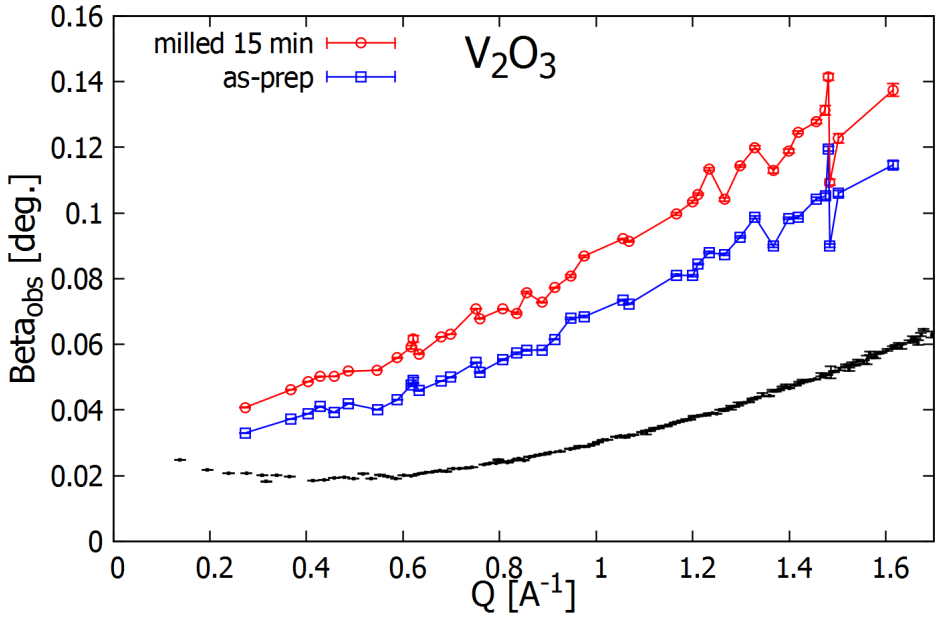

Figure S11: Integral breadths $\beta(Q)$ observed for the Bragg peaks measured with the same V_2O_3 sample before and after milling 15 minutes in planetary mill. Integral breadths $\beta(Q)$ observed for the $Na_2Ca_3Al_2F_{14}$ are presented. The broken lines are shown to guide-the-eye.

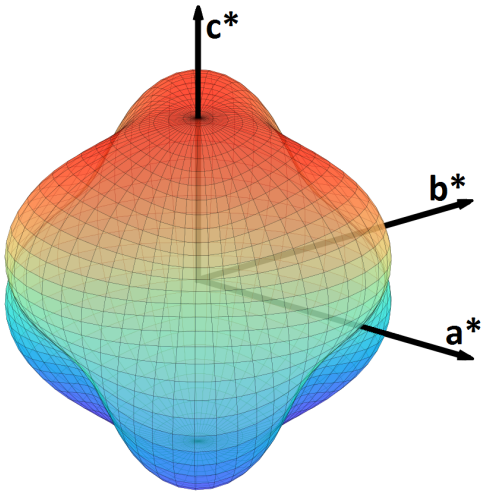

Figure S12: Polar plot of the surface described with the polynomial $W_4(Q, \theta, \varphi)$ i.e. points with radius given as: $R(\theta, \varphi) = 3 + 2\sin^3\theta\cos\theta\cos 3\varphi$ are shown in a 3-dimensional perspective.

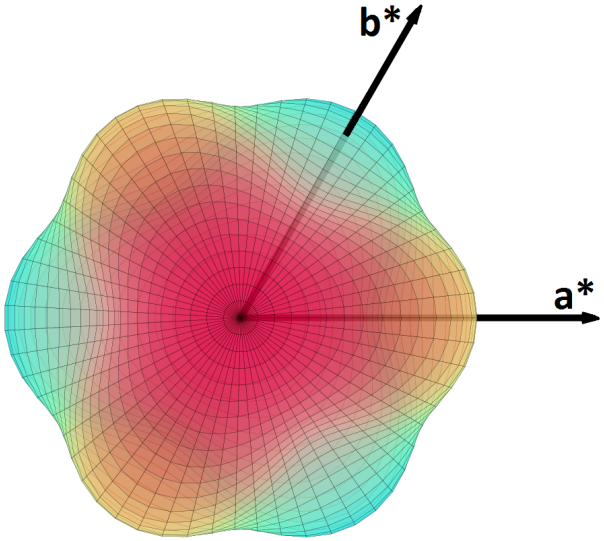

Figure S13: Polar plot of the surface described with the polynomial $W_4(Q, \theta, \varphi)$ i.e. points with radius given as: $R(\theta, \varphi) = 3 + 2\sin^3\theta\cos\theta\cos 3\varphi$ are shown in a 3-dimensional perspective - view along **c** axis.

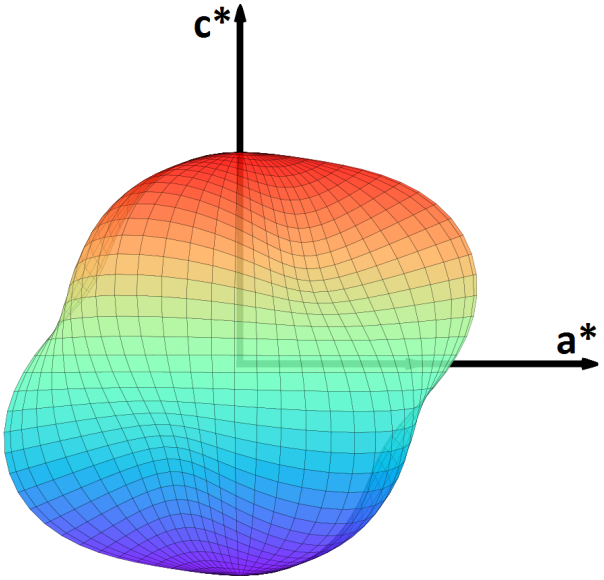

Figure S14: Polar plot of the surface described with the polynomial $W_4(Q, \theta, \varphi)$ i.e. points with radius given as: $R(\theta, \varphi) = 3 + 2\sin^3\theta\cos\theta\cos 3\varphi$ are shown in a 3-dimensional perspective - side view.

Table S1: Comparison of interatomic distances in selected M_2O_3 corundum structures. Upper entries come from this work, lower entries come from literature data (Ti_2O_3[2], V_2O_3[3], Cr_2O_3[4], Al_2O_3[5] α-Fe_2O_3[6]). Labels of ions are the same as in Fig. 8. The unit cell and atomic position parameters are shown in the upper part of the table.

	Ti_2O_3	V_2O_3	Cr_2O_3	Al_2O_3	α-Fe_2O_3
Parameter					
a_h^0 [Å]	5.15941(10) 5.15800(400)	4.95311(11) 4.95150(30)	4.95896(2) 4.95721(3)	4.76002(10) 4.75400(500)	5.03612(3) 5.03550(50)
c_h^0 [Å]	13.60497(35) 13.61100(100)	13.99985(41) 14.00300(100)	13.59477(8) 13.59170(10)	12.99437(37) 12.98200(600)	13.75243(10) 13.74710(70)
x(O)	0.31092(160) 0.31315(6)	0.31110(240) 0.31180(7)	0.30585(60) 0.30569(3)	0.30615(92) 0.30624(9)	0.30640(66) 0.30605(10)
z(M)	0.34463(20) 0.34469(1)	0.34640(28) 0.34629(1)	0.34751(7) 0.34734(3)	0.35219(21) 0.35221(2)	0.35528(6) 0.35522(1)
Distance [Å]					
M_1-O_1	2.0564(67) 2.0664(3)	2.0480(79) 2.0498(3)	2.0144(23) 2.0116(3)	1.9717(36) 1.9698(4)	2.1158(26) 2.1136(4)
M_1-O_5	2.0324(35) 2.0263(2)	1.9718(44) 1.9705(2)	1.9650(12) 1.9656(2)	1.8549(21) 1.8526(3)	1.9432(14) 1.9443(3)
M_1-M_2	2.5741(38) 2.5777(3)	2.7000(59) 2.6967(3)	2.6515(13) 2.6460(6)	2.6559(37) 2.6538(4)	2.8955(12) 2.8929(2)
M_1-M_3	2.9941(4) 2.9940(2)	2.8825(8) 2.8817(1)	2.8891(2) 2.8873(1)	2.7914(6) 2.7881(2)	2.9693(2) 2.9689(2)
M_1-M_4	3.5660(21) 3.5647(2)	3.4710(34) 3.4723(2)	3.4256(7) 3.4268(3)	3.2185(19) 3.2147(3)	3.3620(6) 3.3625(2)
M_1-M_5	3.7433(23) 3.7436(2)	3.6909(38) 3.6904(2)	3.6515(8) 3.6500(4)	3.4988(23) 3.4950(3)	3.7020(7) 3.7016(2)
O_1-O_2	2.7780(100) 2.7977(4)	2.6676(120) 2.6741(4)	2.6268(36) 2.6247(2)	2.5244(52) 2.5216(6)	2.6724(43) 2.6693(6)
O_1-O_3	3.0835(7) 3.0721(2)	2.9596(8) 2.9554(2)	2.9886(3) 2.9878(1)	2.8664(4) 2.8628(3)	3.0316(3) 3.0332(3)
O_1-O_4	2.7846(26) 2.7906(2)	2.8029(30) 2.8044(2)	2.7370(9) 2.7357(1)	2.6199(12) 2.6174(2)	2.7728(10) 2.7715(2)
O_1-O_5	2.8829(32) 2.8796(2)	2.8926(37) 2.8911(2)	2.8482(11) 2.8473(1)	2.7256(16) 2.7227(2)	2.8838(13) 2.8838(2)

Table S2: Comparison of bond angles in selected M_2O_3 corundum structures. Upper entries come from this work, lower entries come from literature data (Ti_2O_3[2], V_2O_3[3], Cr_2O_3[4], Al_2O_3[5] α-Fe_2O_3[6]). Labels of ions are the same as in Fig. 8. The unit cell and atomic position parameters are shown in the upper part of the table.

	Ti_2O_3	V_2O_3	Cr_2O_3	Al_2O_3	α-Fe_2O_3
Parameter					
a_h^0 [Å]	5.15941(10) 5.15800(400)	4.95311(11) 4.95150(30)	4.95896(2) 4.95721(3)	4.76002(10) 4.75400(500)	5.03612(3) 5.03550(50)
c_h^0 [Å]	13.60497(35) 13.61100(100)	13.99985(41) 14.00300(100)	13.59477(8) 13.59170(10)	12.99437(37) 12.98200(600)	13.75243(10) 13.74710(70)
x(O)	0.31092(160) 0.31315(6)	0.31110(240) 0.31180(7)	0.30585(60) 0.30569(3)	0.30615(92) 0.30624(9)	0.30640(66) 0.30605(10)
z(M)	0.34463(20) 0.34469(1)	0.34640(28) 0.34629(1)	0.34751(7) 0.34734(3)	0.35219(21) 0.35221(2)	0.35528(6) 0.35522(1)
Angle [deg.]					
M_1-O_1-M_2	77.492(180) 77.174(7)	82.470(230) 82.265(8)	82.319(68) 82.246(10)	84.677(120) 84.693(12)	86.354(78) 86.371(11)
M_1-O_2-M_3	94.153(210) 94.028(8)	91.606(250) 91.559(9)	93.100(75) 93.088(10)	93.637(130) 93.625(13)	93.934(86) 93.952(13)
M_1-O_5-M_4	122.632(240) 123.198(10)	123.323(310) 123.552(11)	121.302(90) 121.312(11)	120.356(148) 120.368(15)	119.776(110) 119.695(15)
M_1-O_1-M_5	132.554(250) 132.326(10)	133.307(320) 133.250(11)	133.152(94) 133.191(11)	132.203(150) 132.202(15)	131.536(110) 131.573(15)
O_1-M_1-O_2	84.976(200) 85.210(8)	81.273(240) 81.428(8)	81.387(72) 81.442(9)	79.606(120) 79.594(12)	78.328(80) 78.315(12)
O_1-M_1-O_5	89.668(200) 89.427(8)	92.020(250) 91.944(9)	91.398(74) 91.427(10)	90.788(120) 90.794(12)	90.443(84) 90.479(12)
O_5-M_1-O_6	98.679(200) 98.590(8)	97.264(260) 97.169(9)	99.007(75) 98.933(11)	101.191(130) 101.185(13)	102.529(88) 102.526(13)
O_1-M_1-O_6	169.743(210) 170.029(8)	168.405(270) 168.596(9)	167.025(77) 167.113(14)	164.188(140) 164.186(14)	162.289(86) 162.277(13)
O_1-M_1-O_4	85.847(200) 85.972(8)	88.394(250) 88.441(9)	86.900(73) 86.912(10)	86.363(120) 86.375(12)	86.066(84) 86.048(12)

References

[1] Prewitt, C., Shannon, R., Rogers, D. & Sleight, A. (1969). *Inorganic Chem.* **8**, 1985-1993.

[2] Vincent, M., Yvon, K., Gruettner, A. & Ashkenazi, J. (1980b). *Acta Cryst. A*, **36**, 803-808.

[3] Vincent, M., Yvon, K. & Ashkenazi, J. (1980a). *Acta Cryst. A*, **36**, 808-813.

[4] Hill, A., Harrison, A., Dickinson, C., Zhou, W. & Kockelmann, W. (2010). *Microporous and Mesoporous Mater.* **130**, 280-286.

[5] Maslen, E., Streltsov, V., Streltsova, N. & Ishizawa, N. (1993). *Acta Cryst. B*, **49**, 973-980.

[6] Maslen, E., Streltsov, V., Streltsova, N. & Ishizawa, N. (1994). *Acta Cryst. B*, **50**, 435-252.